

# Spin dynamics in a doped-Mott-insulator superconductor

W.Q. Chen and Z.Y. Weng

*Center for Advanced Study, Tsinghua University, Beijing 100084, China*

We present a systematic study of spin dynamics in a superconducting ground state, which itself is a doped-Mott-insulator and can correctly reduce to an antiferromagnetic (AF) state at half-filling with an AF long-range order (AFLRO). Such a doped Mott insulator is described by a mean-field theory based on the phase string formulation of the  $t - J$  model. We show that the well-known spin wave excitation in the AFLRO state at half-filling evolves into a resonancelike peak at a finite energy in the superconducting state, which is located around the AF wave vectors. The width of such a resonancelike peak in momentum space decides a spin correlation length scale which is inversely proportional to the square root of doping concentration, while the energy of the resonancelike peak scales linearly with the doping concentration at low doping. These properties are consistent with experimental observations in the high- $T_c$  cuprates. An important prediction of the theory is that, while the total spin sum rule is satisfied at different doping concentrations, the weight of the resonancelike peak does not vanish, but is continuously saturated to the weight of the AFLRO at zero-doping limit. Besides the low-energy resonancelike peak, we also show that the high-energy excitations still track the spin wave dispersion in momentum space, contributing to a significant portion of the total spin sum rule. The fluctuational effect beyond the mean-field theory is also examined, which is related to the broadening of the resonancelike peak in energy space. In particular, we discuss the incommensurability of the spin dynamics by pointing out that its visibility is strongly tied to the low-energy fluctuations below the resonancelike peak. We finally investigate the interlayer coupling effect on the spin dynamics as a function of doping, by considering a bilayer system.

PACS numbers: 74.20.Mn, 74.25.Ha, 75.40.Gb

## I. INTRODUCTION

The measurement of spin dynamics in the cuprate superconductors is uniquely important. This is because the spin degrees of freedom constitute the predominant part of the low-lying electronic degrees of freedom, *i.e.*,  $1 - \delta$  per site, as compared to the charge degrees of freedom at small hole concentration,  $\delta$ . Such a large imbalance between the spin and charge numbers are usually regarded as a key indicator that the underlying system is a doped Mott insulator<sup>1</sup>. On general grounds, the corresponding spin dynamics is expected to be distinctly different from a conventional BCS superconductor. The latter is based on the Fermi-liquid description in which the elementary excitations are quasiparticles which carry both charge and spin. An extreme case is at half-filling, where the whole charge degrees of freedom get frozen at low energy and only the spin degrees of freedom remain intact in the cuprates, which are well characterized by the Heisenberg model<sup>2</sup>.

Experimentally, anomalous properties of spin dynamics have been observed throughout the cuprate family. The parent compound at half-filling is a Mott insulator in which spins form AFLRO below a Néel temperature  $T_N$ . The elementary excitation is a gapless bosonic Goldstone mode, *i.e.*, the spin wave in the ordered phase. AFLRO and the spin-wave excitation disappear beyond some critical concentration of holes introduced into the system. Except for some residual signature of spin waves at high energies, the low-lying spin-wave-type excitation is completely absent once the system becomes a superconductor. It is replaced by a resonancelike peak at a doping-dependent energy around the AF wave vector  $\mathbf{Q}_{AF} = (\pi, \pi)$ , as observed first in the optimal doped YBCO compound<sup>3,4</sup>, where the dynamic spin susceptibility function measured by inelastic neutron scattering shows a sharp peak at  $\omega_{res} = 41$  meV, whose width is comparable to the resolution limit of the instruments. Similar resonancelike peak has also been observed in the underdoped YBCO compounds<sup>5</sup> (where the resonancelike peak persists into the pseudogap phase above the superconducting transition), Tl-based<sup>6</sup> and Bi-based<sup>7</sup> compounds. In the LSCO compound, although no such a sharp peak has been found, the low-lying spin excitation is nonetheless non spin-wave-like, which may be still regarded as a very broad peak in energy space<sup>8</sup>. With much sharper linewidth in momentum space, doping-dependent incommensurate splittings around  $\mathbf{Q}_{AF}$  have been clearly identified in LSCO<sup>9,10</sup>. Similar incommensurability, even though not as prominent as in LSCO, has been also established in underdoped YBCO recently<sup>11-13</sup>.

Theoretically, a great challenge is how to naturally connect the spin dynamic at half-filling with that in the superconducting phase in which the doping concentration can be as low as a few percent per Cu site. That is, although the low-energy, long-wavelength behavior may change qualitatively in the superconducting phase, the number of spins in the background is still quite close to half-filling, which far exceeds the number of doped holes. Physically it is very

hard to imagine that the *short-range, high-energy* spin correlations would be changed completely by a few percent to ten percent doping. However, in a BCS superconductor, the upper spin energy scale is usually set by the Fermi energy  $\epsilon_f$ <sup>14</sup>, such that in the local spin susceptibility one has to integrate over the frequency up to  $\epsilon_f$  in order to recover the correct sum rule of  $1 - \delta$  spin per site. Normally  $\epsilon_f$  is much larger than  $J$ . Thus, why there should be a gigantic increase in the upper spin energy in the doped case, compared to the half-filling, poses a serious challenge to any approach based on the d-wave BCS-type theory in which the spin dynamic is solely contributed by quasiparticle excitations. Experimentally the upper energy scale exhibited in the dynamic spin susceptibility is set by  $\sim 2J$  ( $J$  is the superexchange coupling) at half-filling, in consistency with the prediction by the Heisenberg model, and is slightly reduced in the optimal-doped superconducting phase<sup>8</sup>. No trace of any other new high-energy scale has been ever reported in the doped regime in spin channels.

As for the low-energy feature, like the resonancelike peak structure observed in the experiments, theoretical proposals are ranged from the RPA fluctuations in the particle-hole channel within the framework of BCS<sup>14</sup> or generalized BCS theories<sup>15,16</sup> to some novel mechanism of the so-called  $\pi$  mode in the particle-particle channel in the SO(5) theory<sup>17</sup>, which is coupled to the particle-hole channel in the superconducting phase. An important question, not being properly addressed yet, is what is the connection, if any, of such a resonancelike spin mode with the spin wave in the zero-doping limit. Namely, how a few percent of doped holes can continuously reshape a spin-wave excitation into a non-propagating local mode, with an AFLRO turning into short-range spin correlations. This question and the previous high-energy one constitute two of most fundamental issues in an approach based on doped Mott insulators.

In this paper, we put forward a systematic description of the evolution of spin dynamics as a function of doping in a doped-Mott-insulator superconductor. It is described by a bosonic resonating-valence-bond (RVB) mean-field theory<sup>18</sup> based on the phase-string formulation<sup>19</sup> of the  $t - J$  model. At half-filling, the mean-field theory reduces to the Schwinger-boson mean-field state<sup>20</sup>, which well characterizes AFLRO and spin-wave excitations in the ground state. At finite doping, the mean-field theory depicts how the spin dynamics is influenced by the doping effect in going into the superconducting state. In particular, we show how a resonancelike peak centered around  $\mathbf{Q}_{AF}$  emerges out of spin waves from the AFLRO phase. A unique prediction for experiment is that the weight of the resonancelike peak continuously evolves into that of the AFLRO in the zero-doping limit. On the other hand, the total weight of the dynamic susceptibility function, which extends slightly over  $\sim 2J$  in energy, still satisfies the sum rule that the total spin number is  $1 - \delta$  per site.

In this unified mean-field description, doping-dependent resonancelike energy and spin correlation length are quantitatively determined. Besides the low-energy resonancelike peak structure near  $\mathbf{Q}_{AF}$ , there still exists a high-energy spectrum whose envelope roughly tracks the spin wave dispersion as a residual effect in the superconducting phase. We also consider some important fluctuational effect beyond the mean-field theory on the lineshape of the spectral function, and discuss the incommensurability and its visibility in this framework. We finally introduce the interlayer superexchange coupling and investigate how the spin dynamics changes in the even and odd channels for a double-layer system. Comparisons with the experimental measurements, mostly by inelastic neutron scattering, are made.

The remainder of the paper is organized as follows. In Sec. II, a systematic study of the spin dynamics in the bosonic RVB mean-field state for the single-layer system is presented. In Sec. III, fluctuational effects beyond the mean-field theory, due to the charge density fluctuations, are discussed. In Sec. IV, the interlayer coupling for a bilayer system is considered. Finally, a summary is given in Sec. V.

## II. SPIN DYNAMICS IN MEAN FIELD DESCRIPTION

### A. Bosonic RVB state at half-filling

Spin dynamics of the cuprates at half-filling is well described by the two-dimensional (2D) AF Heisenberg model. Although a conventional spin-wave theory is quite successful in understanding the low-lying excitation spectrum of the Heisenberg Hamiltonian, to make the theory applicable or modifiable to the cases without AFLRO, like at finite temperatures or in doped regimes, we shall use the Schwinger-boson formulation as our starting point at half-filling.

The mean-field theory<sup>20</sup> based on the Schwinger-boson formulation can characterize the AFLRO and spin-wave excitation fairly well in the ground state. Its mean-field wavefunction under the Gutzwiller projection will have the same form<sup>21</sup> as the variational bosonic RVB wavefunctions proposed by Liang, Doucot, and Anderson<sup>22</sup>. The latter can produce very accurate variational energies as well as the AF magnetization for the Heisenberg model, indicating that the state correctly captures *both* long-range and short-range spin correlations. Such an approach is thus called bosonic RVB description, which is to be generalized to finite doping in the next subsection. In the following, we briefly review some basic equations of the bosonic RVB mean-field theory at half-filling.

In the Schwinger-boson formulation, the spin operators can be expressed by the Schwinger-boson operator  $b_{i\sigma}$  as follows

$$S_i^+ = (-1)^i b_{i\uparrow}^\dagger b_{i\downarrow}, \quad (1)$$

(note that a staggered sign factor  $(-1)^i$  is explicitly introduced here in contrast to the original definition<sup>20</sup>), and  $S_i^- = (S_i^+)^\dagger$ , while  $S_i^z = \sum_\sigma \sigma b_{i\sigma}^\dagger b_{i\sigma}$ . The Schwinger bosons satisfy the constraint  $\sum_\sigma b_{i\sigma}^\dagger b_{i\sigma} = 1$ . The mean-field state is characterized by the bosonic RVB order parameter

$$\Delta_0^s = \sum_\sigma \langle b_{i\sigma} b_{j-\sigma} \rangle, \quad (2)$$

which leads to the following effective Hamiltonian, obtained from the half-filling  $t - J$  (Heisenberg) model:

$$H_s = -\frac{J\Delta_0^s}{2} \sum_{\langle ij \rangle \sigma} b_{i\sigma}^\dagger b_{j-\sigma}^\dagger + H.c. + \text{const.} + \lambda \left( \sum_{i\sigma} b_{i\sigma}^\dagger b_{i\sigma} - N \right), \quad (3)$$

where the last term involves a Lagrangian multiplier  $\lambda$  to enforce the global constraint of total spinon number,  $\sum_{i\sigma} b_{i\sigma}^\dagger b_{i\sigma} = N$ .

The mean-field Heisenberg Hamiltonian (3) can be straightforwardly diagonalized by the Bogoliubov transformation

$$b_{i\sigma} = \sum_{\mathbf{k}} \omega_{\mathbf{k}\sigma}(i) (u_{\mathbf{k}} \gamma_{\mathbf{k}\sigma} - v_{\mathbf{k}} \gamma_{\mathbf{k}-\sigma}^\dagger), \quad (4)$$

as

$$H_s = \sum_{\mathbf{k}\sigma} E_{\mathbf{k}} \gamma_{\mathbf{k}\sigma}^\dagger \gamma_{\mathbf{k}\sigma}. \quad (5)$$

Here,  $\omega_{\mathbf{k}\sigma}(i) = \frac{1}{\sqrt{N}} e^{i\sigma \mathbf{k} \cdot \mathbf{r}_i}$ , and the coherent factors,  $u_{\mathbf{k}}$  and  $v_{\mathbf{k}}$ , are given by

$$u_{\mathbf{k}} = \frac{1}{\sqrt{2}} \sqrt{\frac{\lambda}{E_{\mathbf{k}}} + 1}, \quad v_{\mathbf{k}} = \frac{\text{sgn}(\xi_{\mathbf{k}})}{\sqrt{2}} \sqrt{\frac{\lambda}{E_{\mathbf{k}}} - 1}, \quad (6)$$

where  $\xi_{\mathbf{k}} = -J\Delta_0^s(\cos k_x a + \cos k_y a)$  and

$$E_{\mathbf{k}} = \sqrt{\lambda^2 - \xi_{\mathbf{k}}^2}. \quad (7)$$

Finally, in a self-consistent manner, the RVB order parameter  $\Delta_0^s$  and the Lagrangian multiplier  $\lambda$  are determined by the following self-consistent equations

$$|\Delta_0^s|^2 = \frac{1}{2N} \sum_{\mathbf{k}} \frac{\xi_{\mathbf{k}}^2}{JE_{\mathbf{k}}} \coth \frac{\beta E_{\mathbf{k}}}{2}, \quad (8)$$

$$2 = \frac{1}{N} \sum_{\mathbf{k} \neq 0} \frac{\lambda}{E_{\mathbf{k}}} \coth \frac{\beta E_{\mathbf{k}}}{2} + n_{BC}^b, \quad (9)$$

in which  $n_{BC}^b$  is the contribution from the Bose condensation of the Schwinger bosons, leading to an AFLRO, which happens if  $E_{\mathbf{k}}$  becomes gapless. Note that  $\beta = 1/T$  and the AFLRO disappears ( $n_{BC}^b = 0$ ) at a finite temperature  $T$ .

## B. Bosonic RVB description at finite doping

Although AF correlations at half-filling are well captured by the mean-field Hamiltonian  $H_s$  in (3), the doping effect on the spin background is a highly nontrivial issue.

Based on the phase-string formulation<sup>19</sup>, which is an exact reformulation by sorting out the most singular doping effect, *i.e.*, the phase string effect in the  $t - J$  model, a generalized mean-field Hamiltonian describing the spin degrees of freedom can be obtained<sup>18</sup> as follows

$$H_s = -\frac{J\Delta^s}{2} \sum_{\langle ij \rangle \sigma} b_{i\sigma}^\dagger b_{j-\sigma}^\dagger e^{i\sigma A_{ij}^h} + H.c. + \text{const.} + \lambda \left( \sum_{i\sigma} b_{i\sigma}^\dagger b_{i\sigma} - (1-\delta)N \right). \quad (10)$$

Compared to the half-filling case,  $H_s$  in (10) differs from (3) mainly by the emergence of a gauge field  $A_{ij}^h$  defined on the nearest-neighboring (NN) link  $(ij)$ , satisfying the following constraint

$$\sum_{\langle ij \rangle \in c} A_{ij}^h = \pi \sum_{l \in \Omega_c} n_l^h, \quad (11)$$

where  $c$  is a, say, counter-clockwise-oriented, close loop and  $\Omega_c$  is the area enclosed by  $c$ . On the right-hand-side (rhs) of (11),  $n_l^h$  denotes the number operator of doped holes at site  $l$ . Therefore, the doping effect explicitly enters in (10) through the gauge field  $A_{ij}^h$  as if each hole carries a fictitious  $\pi$  fluxoid as seen by spinons in  $H_s$ . In (10), the bosonic RVB order parameter is given by

$$\Delta^s = \sum_{\sigma} \left\langle e^{-i\sigma A_{ij}^h} b_{i\sigma} b_{j-\sigma} \right\rangle_{NN} \quad (12)$$

for NN sites  $i$  and  $j$ . At half filling, because there is no hole, it is obvious that  $A_{ij}^h = 0$ , and  $\Delta^s$  reduces back to  $\Delta_0^s$  defined in (2).

Note that the doping concentration  $\delta$  also enters  $H_s$  through the Lagrangian multiplier  $\lambda$  which implements the global condition  $\sum_{i\sigma} b_{i\sigma}^\dagger b_{i\sigma} = (1-\delta)N$ . But at low doping, the effect of missing spins from such a term will be far less dramatic than the topological gauge field  $A_{ij}^h$ . The latter reflects the singular phase string effect<sup>19</sup> induced by the hopping of doped holes on the AF spin background.

Corresponding to  $H_s$  in (10), the spin operators in the phase string formulation<sup>19</sup> read

$$S_i^+ = (-1)^i e^{i\Phi_i^h} b_{i\uparrow}^\dagger b_{i\downarrow}, \quad (13)$$

$S_i^- = (S_i^+)^{\dagger}$ , and  $S_i^z = \sum_{\sigma} \sigma b_{i\sigma}^\dagger b_{i\sigma}$ , respectively. Compared to the Schwinger-boson formulation in (1), an extra phase  $\Phi_i^h$  appears in (13), which satisfies  $\Phi_i^h - \Phi_j^h = 2A_{ij}^h$  ( $ij \in \text{spin sites}$ ) and ensures the spin rotational symmetry of the effective Hamiltonian (10).

Equation (10) is by nature a gauge model. But in the superconducting ground state, due to the Bose condensation of bosonic holons in the bosonic RVB theory<sup>18</sup>, the spin Hamiltonian  $H_s$  will become quite simplified as  $A_{ij}^h$  can be approximately treated as describing a uniform flux with a strength

$$\sum_{\square} A_{ij}^h = \pi\delta. \quad (14)$$

Then we can introduce the following Bogoliubov transformation to diagonalize (10), just like (4) to (3),

$$b_{i\sigma} = \sum_m \omega_{m\sigma}(i) (u_m \gamma_{m\sigma} - v_m \gamma_{m-\sigma}^\dagger). \quad (15)$$

With a standard procedure, we obtain

$$H_s = \sum_{m\sigma} E_m \gamma_{m\sigma}^\dagger \gamma_{m\sigma}, \quad (16)$$

with the spinon spectrum

$$E_m = \sqrt{\lambda^2 - \xi_m^2}. \quad (17)$$

In this scheme,  $\xi_m$  and  $\omega_{m\sigma}(i) = \omega_{m-\sigma}^*(i)$  are eigenvalues and eigenfunctions of the following equation

$$\xi_m \omega_{m\sigma}(i) = -\frac{J\Delta^s}{2} \sum_{j=NN(i)} e^{i\sigma A_{ij}^h} \omega_{m\sigma}(j). \quad (18)$$

and the coherent factors,  $u_m$  and  $v_m$ , are given by

$$u_m = \frac{1}{\sqrt{2}} \sqrt{\frac{\lambda}{E_m} + 1}, \quad v_m = \text{sgn}(\xi_m) \frac{1}{\sqrt{2}} \sqrt{\frac{\lambda}{E_m} - 1}. \quad (19)$$

Finally,  $\lambda$  and  $\Delta^s$  can be determined by the self-consistent equations

$$|\Delta^s|^2 = \frac{1}{2NJ} \sum_m \frac{\xi_m^2}{E_m} \coth \frac{\beta E_m}{2}, \quad (20)$$

$$2 - \delta = \frac{1}{N} \sum_{m \neq 0} \frac{\lambda}{E_m} \coth \frac{\beta E_m}{2} + n_{BC}^b. \quad (21)$$

Here  $n_{BC}^b$  is the contribution of the condensation of spinons, if an AFLRO exists like in the half-filling case.

The above mean-field formulation is essentially the same as the one outlined in Ref.<sup>18</sup>. For simplicity and clarity, here we have not introduced an approximate doping-correction factor in (20) ( $\approx 1 - 2\delta$ ) as we will be mainly concerned with the evolution of spin dynamics at low doping. A spin feedback effect from the hopping term is not included either, which results in a shift of  $\lambda$  to  $\lambda_m$  in  $E_m$ <sup>18</sup>, without qualitatively changing the physical consequences.

### C. Spin dynamics in superconducting ground state

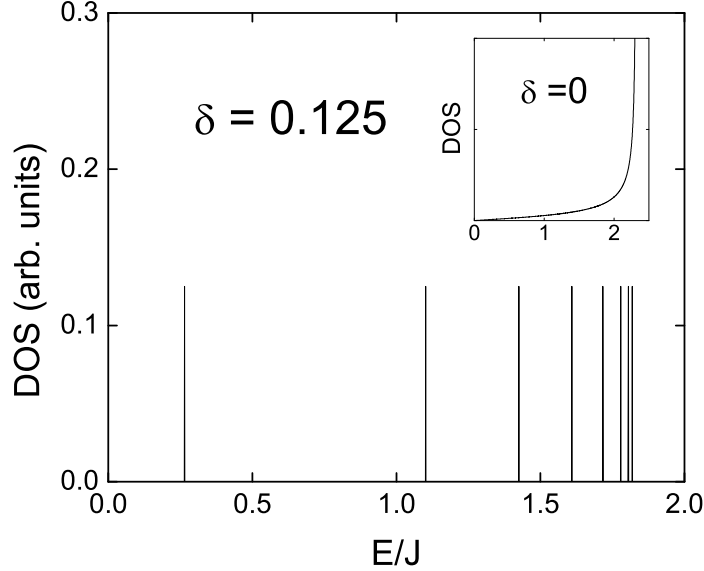


FIG. 1: The density of states (DOS) of the mean-field spinon spectrum  $E_m$  at doping  $\delta = 0.125$ . Inset: the DOS in the AF state at half filling.

#### 1. Excitation spectrum $E_m$

According to the mean-field scheme outlined above, we can numerically determine the mean-field ‘spinon’ spectrum  $E_m$  defined in (17).

As an example, we solve the eigenequation (18) and self-consistent equations (20) and (21) at doping concentration  $\delta = 0.125$ . The chemical potential  $\lambda$  is found to be  $1.819J$  while the RVB order parameter  $\Delta^s$  is  $0.993$ . In contrast, at half filling, the results are  $\lambda = 2.316J$  and  $\Delta_0^s = 1.158$ .

In Fig. 1, the density of states (DOS) of the spectrum  $E_m$  for  $\delta = 0.125$  is shown in the main panel, while the half-filling case is plotted in the inset for comparison. The figure shows that the two spectra are qualitatively very different. At half-filling, the spectrum is continuous and gapless, with a large density of states at the maximal energy which is slightly above  $2J$ . In the superconducting state, the spectrum becomes discretized levels. This discrete levels are due to the fact that the spectrum  $\xi_m$  as the solution of (18) has a Hofstadter spectrum as the result of the vector potential  $A_{ij}^h$  given in (14). Note that the distribution of the Landau-level-like structure in Fig. 1 remains uneven, which reflects the fact that the average density of states increases with energy, as seen at half-filling. The maximal energy is slightly less than  $2J$  at  $\delta = 0.125$ .

It is important to note that there is a gap between the lowest discrete level and zero energy, which is  $\sim 0.265J$  for  $\delta = 0.125$ . There will no more spinon Bose condensation  $n_{BC}^b \neq 0$  such that the AFLRO no longer exists.

## 2. Dynamic spin susceptibility

After diagonalizing the effective Hamiltonian  $H_s$ , the spin susceptibility can be obtained straightforwardly. Due to the spin rotational invariance<sup>18</sup>, one may only consider the  $\hat{z}$ -component susceptibility, which can be derived based on the Matsubara Green's function  $-\langle T_\tau S_j^z(\tau) S_i^z(0) \rangle$ . With the standard procedure outlined in Ref.<sup>18</sup>, the imaginary part of the dynamic spin susceptibility at zero temperature is given by

$$\chi''(\mathbf{Q}, \omega) = \frac{\pi}{8} \sum_{mm'} C_{mm'}(\mathbf{Q}) \left( \frac{\lambda^2 - \xi_m \xi_{m'}}{E_m E_{m'}} - 1 \right) \text{sgn}(\omega) \delta(|\omega| - E_m - E_{m'}), \quad (22)$$

where

$$C_{mm'}(\mathbf{Q}) \equiv \frac{1}{N} \sum_{ij} e^{i\mathbf{Q} \cdot (\mathbf{x}_i - \mathbf{x}_j)} \omega_{m\sigma}(i) \omega_{m\sigma}^*(j) \omega_{m'\sigma}^*(i) \omega_{m'\sigma}(j). \quad (23)$$

The discrete energy levels of  $E_m$  illustrated in Fig.1 will show up in  $\chi''(\mathbf{Q}, \omega)$ . We plot the positions of these peaks in  $\chi''(\mathbf{Q}, \omega)$  in energy and momentum space, as well as the FWHM (full width of half maximum) in momentum space, in Fig. 2. The momentum scan in Fig. 2(a) is along  $(\pi, q)$  direction and is along the diagonal  $(q, q)$  in Fig. 2(b). One sees that each discrete energy corresponds to a finite width in momentum as depicted by a finite bar.

For comparison, the spin-wave peak positions at half-filling are shown as dotted curves in Fig.2. At  $\delta = 0.125$ , although the spin excitations are no longer propagating modes, as evidenced by the flat (dispersionless) small bars at discrete energies, the envelope of the overall spectrum at high energies still approximately track the dispersion of the spin wave at half-filling, with a slightly softened spin-wave velocity. Note that there are actually some more peaks at even higher energies than in Fig.2, but their weight is much reduced due to the coherent factors in  $\chi''(\mathbf{Q}, \omega)$  (see the local spin susceptibility below).

Fig.2 clearly depicts how the spin excitations in the superconducting state continuously evolves from the spin-wave picture at half-filling. The remnant high-energy spin wave signature at finite doping is a very unique feature in this approach. In the following, we turn our attention to the lowest peak in Fig.2, which has the largest weight as marked by the darkest FWHM bar.

## 3. Resonancelike peak around AF wave-vector $\mathbf{Q}_{AF}$

Let us consider two special momenta,  $\mathbf{Q}_0 = (0, 0)$  and  $\mathbf{Q}_{AF} = (\pi, \pi)$ . For  $\mathbf{Q} = \mathbf{Q}_0$ , with the relation  $\sum_i \omega_{m\sigma}(i) \omega_{m'\sigma}^*(i) = \delta_{mm'}$ , we have  $C_{mm'}(\mathbf{Q}_0) = \frac{1}{N} \delta_{mm'}$  such that

$$\chi''(\mathbf{Q}_0, \omega) = \frac{\pi}{8N} \sum_m \left( \frac{\lambda^2 - \xi_m^2 - E_m^2}{E_m^2} \right) \text{sgn}(\omega) \delta(|\omega| - 2E_m) = 0.$$

Namely, there is no signature of  $\chi''(\mathbf{Q}, \omega)$  at the ferromagnetic momentum  $\mathbf{Q}_0$ .

At the AF momentum  $\mathbf{Q}_{AF}$ , one has

$$C_{mm'}(\mathbf{Q}_{AF}) = \frac{1}{N} \sum_{ij} (-1)^{i-j} \omega_{m\sigma}(i) \omega_{m\sigma}^*(j) \omega_{m'\sigma}^*(i) \omega_{m'\sigma}(j). \quad (24)$$

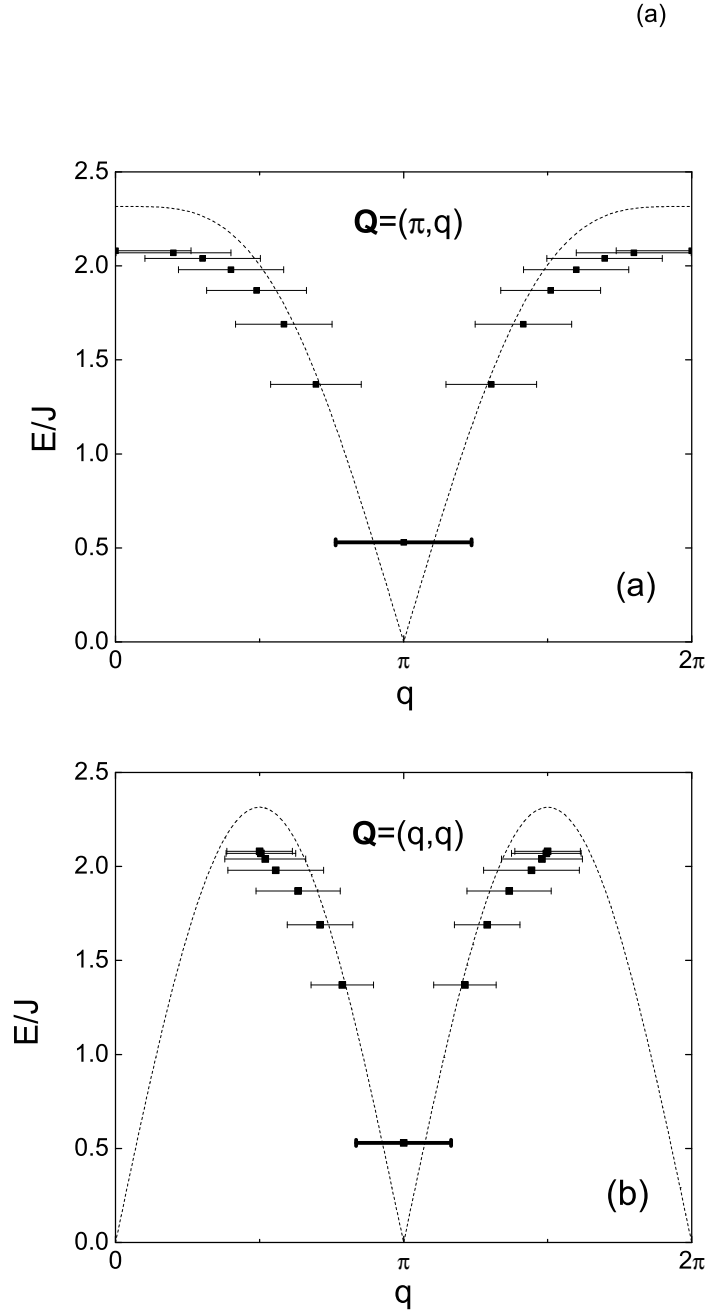


FIG. 2: The dispersive behavior of the spin excitation in the superconducting state ( $\delta = 0.125$ ), in comparison with the spin-wave dispersion at half-filling (dashed curve). The peak positions of  $\chi''$  in  $\mathbf{Q}$ - and  $\omega$ -space are shown along different  $\mathbf{Q}$ -directions: (a) along the diagonal direction,  $\mathbf{Q} = (q, q)$ ; (b) along  $\mathbf{Q} = (\pi, q)$ . The solid bars mark the widths of the peaks in the momentum space (see text).

In the eigenequation (18), it can be easily shown that for any given state  $m$  there is a corresponding state  $\bar{m}$  with the relation  $\xi_m = -\xi_{\bar{m}}$  and  $\omega_{m\sigma}(i) = (-1)^i \omega_{\bar{m}\sigma}(i)$ . Then (24) is reduced to

$$C_{mm'}(\mathbf{Q}_{\text{AF}}) = \frac{1}{N} \sum_{ij} \omega_{m\sigma}(i) \omega_{m\sigma}^*(j) \omega_{\bar{m}'\sigma}^*(i) \omega_{\bar{m}'\sigma}(j) = \frac{1}{N} \delta_{m\bar{m}'}.$$

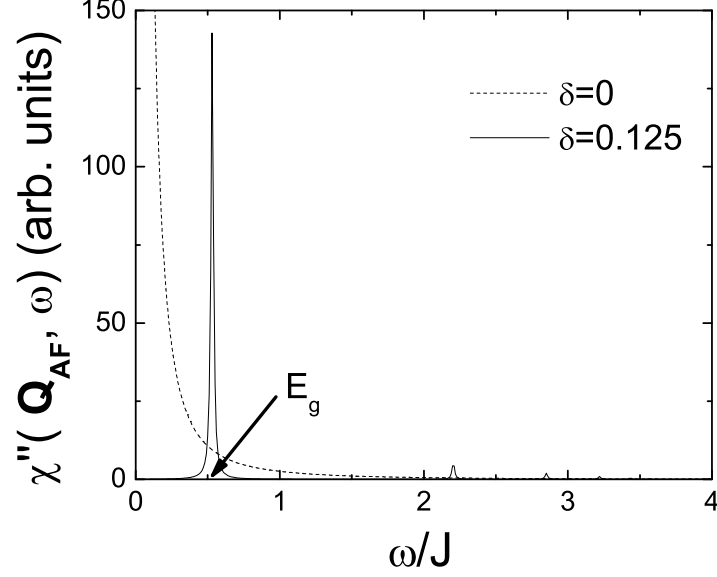


FIG. 3: Dynamic spin susceptibility  $\chi''(\mathbf{Q}_{\text{AF}} = (\pi, \pi), \omega)$  in the superconducting phase with  $\delta = 0.125$  (solid curve).  $E_g$  denotes the position of the resonancelike peak. The dotted curve is for the AF state at half filling.

and the dynamic spin susceptibility at  $\mathbf{Q}_{\text{AF}}$  can be simplified to

$$\chi''(\mathbf{Q}_{\text{AF}}, \omega) = \frac{\pi}{4N} \sum_m \left( \frac{\xi_m^2}{E_m^2} \right) \text{sgn}(\omega) \delta(|\omega| - 2E_m). \quad (25)$$

The numerical result of  $\chi''(\mathbf{Q}_{\text{AF}}, \omega)$  at  $\delta = 0.125$  is shown in Fig. 3 by the solid curve. The dotted curve is calculated at half-filling, which diverges as  $1/\omega^2$  at  $\omega \rightarrow 0$ , in consistency with the spin-wave theory. Thus, in the superconducting phase, a resonancelike peak appears at  $\mathbf{Q}_{\text{AF}}$  with a finite energy  $E_g = 0.53J$  at 0.125 (twice bigger than that of  $E_m$  shown in Fig.1). Note that higher energy (harmonic) peaks in  $\chi''(\mathbf{Q}_{\text{AF}}, \omega)$  are greatly reduced in strength in Fig.3 due to the coherence factor  $\frac{\xi_m^2}{E_m^2}$  in (25). So only the lowest peak at  $E_g$  is clearly exhibited around  $\mathbf{Q}_{\text{AF}}$ .

We further plot the resonancelike peak energy  $E_g$  as a function of hole concentration in Fig. 4. At small doping,  $E_g$  is linearly proportional to  $\delta$ ,  $E_g = 3.336J\delta$ , which is extrapolated to zero at half-filling, where the gapless spin wave is recovered.

The momentum profile of the resonancelike peak at  $E_g$  is shown in a three-dimensional plot in Fig. 5 at  $\delta = 0.125$ . It shows an intrinsic broadening of  $\chi''(\mathbf{Q}, E_g)$  in momentum around  $\mathbf{Q}_{\text{AF}}$ , which can be well fit by a Gaussian distribution function

$$\chi''(\mathbf{Q}, E_g) \propto \exp\left(-\frac{(\mathbf{Q} - \mathbf{Q}_{\text{AF}})^2}{2\sigma^2}\right). \quad (26)$$

The results for different hole concentrations are given in Fig. 6(a) along the diagonal momenta  $\mathbf{Q} = (q, q)$ . One can adjust  $\sigma$  to make all data well collapse onto a single Gaussian function of (26) as shown in the inset of Fig. 6(a). The obtained broadening  $\sigma$  turns out to be nicely scaled linearly with  $\sqrt{\delta}$  [see in Fig. 6(b)]. Similar plots can be done along different  $\mathbf{Q}$  scans centered at  $\mathbf{Q}_{\text{AF}}$  and generally one has  $\sigma \propto \sqrt{\delta}$  in all directions.

If we neglect the small anisotropy along different momentum directions centered at  $\mathbf{Q}_{\text{AF}}$  and perform a Fourier transformation to (26), we obtain the real-space correlation

$$\chi''(\mathbf{R}, \omega) \propto \exp\left(-\frac{\sigma^2 \mathbf{R}^2}{2}\right) \equiv \exp\left(-\frac{\mathbf{R}^2}{\xi^2}\right) \quad (27)$$



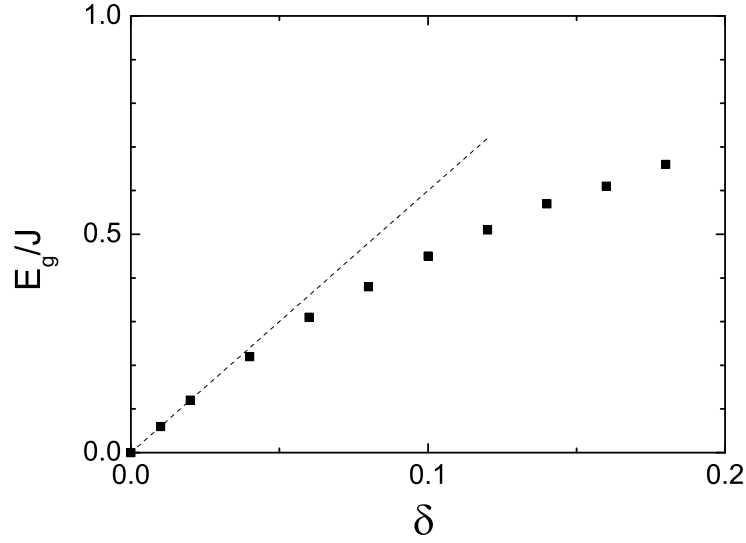


FIG. 4: The doping dependence of the resonancelike peak energy  $E_g$ . The dashed line illustrates the linear doping dependence at small  $\delta$ .

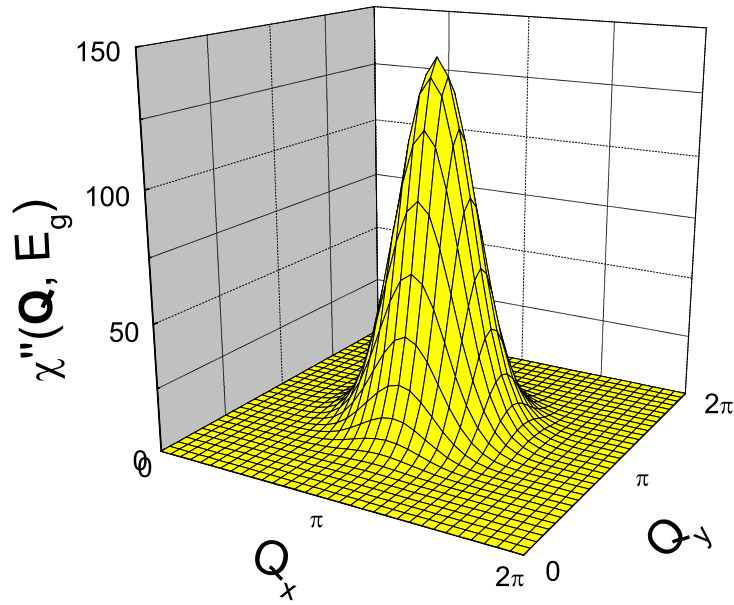


FIG. 5: Momentum distribution of  $\chi''(\mathbf{Q}, \omega)$  at  $\omega = E_g$  ( $\delta = 0.125$ ).

with  $\xi = \frac{\sqrt{2}}{\sigma}$ . Thus, the spin-spin correlation function decays exponentially with the distance in the superconducting phase. This is consistent with a spin gap  $E_g$  opening up in the spin excitation spectrum. In Fig. 7,  $\xi$  is well fit by the solid curve

$$\xi = a \sqrt{\frac{2}{\pi \delta}}. \quad (28)$$

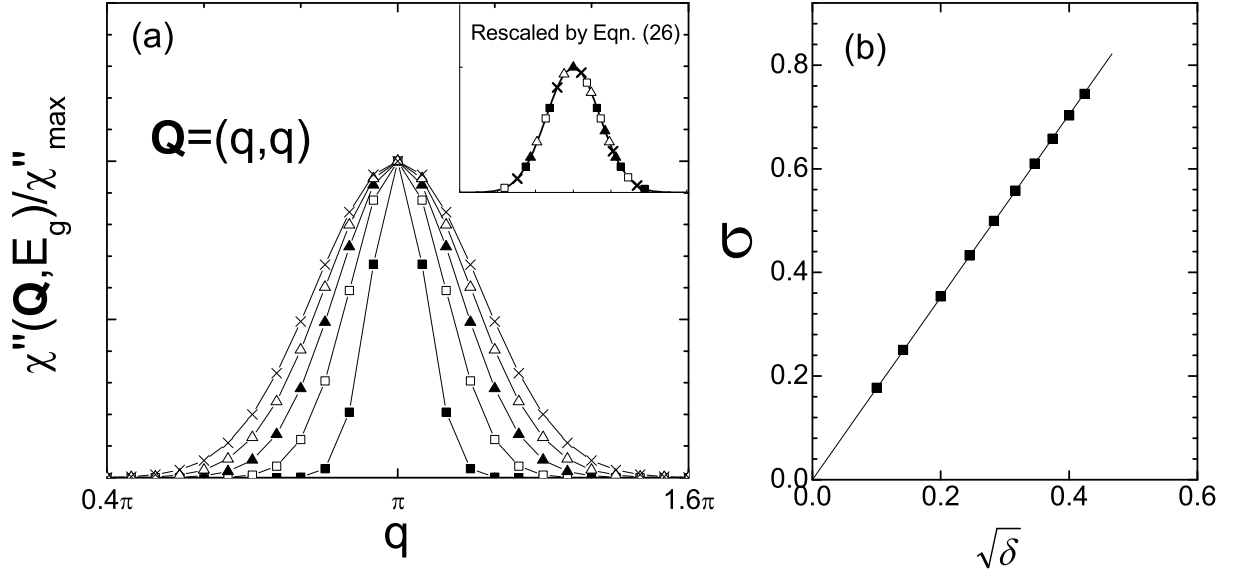


FIG. 6: (a) Momentum distribution of  $\chi''(\mathbf{Q}, E_g)$ , scanned along the diagonal direction  $\mathbf{Q} = (q, q)$  at various hole concentrations. The intensities are normalized at the maximums. The inset shows that the data in the main panel can be well fit into a Gaussian function  $\exp(-(\mathbf{Q} - \mathbf{Q}_{AF})^2/2\sigma^2)$ , with  $\sigma$  being scaled as linearly proportional to  $\sqrt{\delta}$ , as shown in (b).

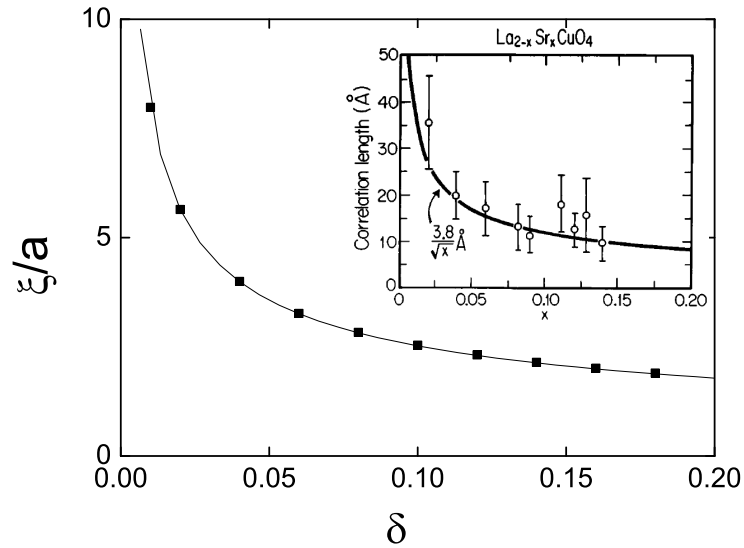


FIG. 7: The relation between the spin correlation length  $\xi/a$  and the hole concentration  $\delta$ . The solid curve is  $\frac{2}{\pi\sqrt{\delta}}$ . The inset is the experimental results given in Ref.<sup>9</sup>.

In the inset, the experimental result obtained in LSCO<sup>9</sup> is presented for comparison. The general trend of  $\xi/a \propto 1/\sqrt{\delta}$  in both the experiment and theory is quite telling.

In Sec. III, we shall further discuss the momentum profile and longer spin correlation lengths at *lower* energies, related to those seen in the LSCO compound<sup>9,10</sup>, when the fluctuation effect is considered.

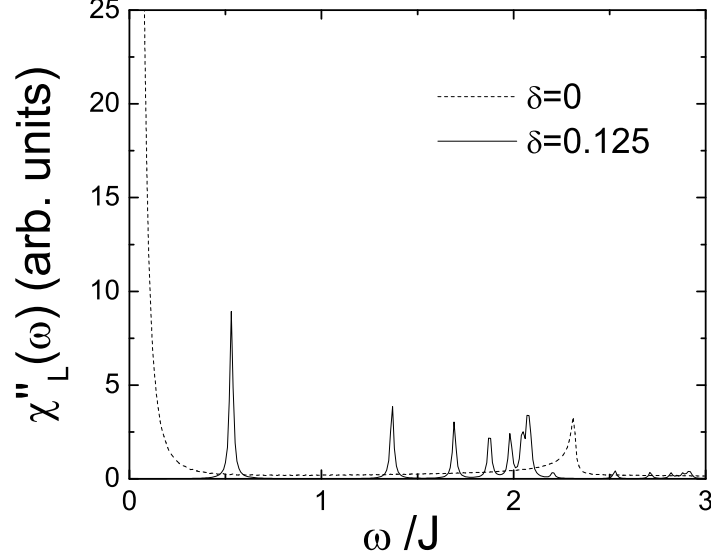


FIG. 8: Local susceptibility  $\chi_L''(\omega)$  in the superconducting phase (solid curve) with  $\delta = 0.125$ , and at half filling (dashed curve).

#### 4. Local susceptibility and spin sum rule

The local spin susceptibility  $\chi_L''(\omega)$  is also an important quantity. It is defined by

$$\chi_L''(\omega) = \int \frac{d^2\mathbf{Q}}{(2\pi)^2} \chi''(\mathbf{Q}, \omega),$$

which describes the on-site spin-spin correlation. Based on (22), one obtains

$$\chi_L''(\omega) = \frac{\pi}{8} \sum_{mm'} K_{mm'} \left( \frac{\lambda^2}{E_m E_{m'}} - 1 \right) \text{sgn}(\omega) \delta(|\omega| - E_m - E_{m'}), \quad (29)$$

where

$$K_{mm'} \equiv \frac{1}{N} \sum_i |\omega_{m\sigma}(i)|^2 |\omega_{m'\sigma}(i)|^2. \quad (30)$$

The numerical results of  $\chi_L''(\omega)$  at  $\delta = 0.125$  and  $\delta = 0$  are presented in Fig.8 by the solid and dashed curves, respectively. The low-energy parts in both cases are similar to those seen in  $\chi''(\mathbf{Q}, \omega)$  around  $\mathbf{Q}_{\text{AF}}$  (Fig. 3), as the AF correlations are dominant at low energies. At high energies, more excitations which in momentum space disperse away from  $\mathbf{Q}_{\text{AF}}$ , as shown in Fig.2, are clearly present in  $\chi_L''(\omega)$ . We see that the main band extends up to  $\sim 2.3J$  at half-filling, while is slightly reduced to around  $\sim 2.1J$  at  $\delta = 0.125$ . These upper-bound spin excitations are expected to be seen near the Brillouin zone boundary (see Fig.2).

Although the intensity of each peak is physically not very meaningful, the weigh of the peak is. The reason is that there is a sum rule about the local dynamic spin susceptibility:

$$W_{\text{total}} \equiv \int d\omega [1 + n(\omega)] \chi_L''(\omega) = \langle (S_i^z)^2 \rangle, \quad (31)$$

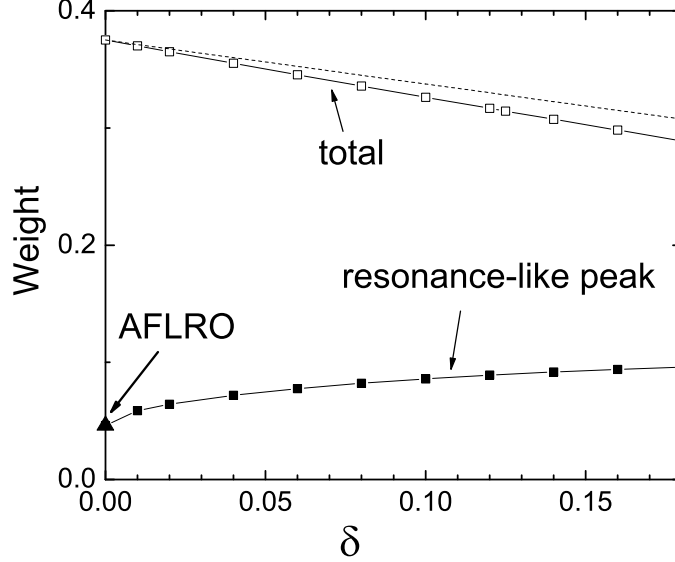


FIG. 9: The spin spectral weight vs doping. Open squares: the total weight; close squares: the weight of the resonancelike peak around  $\mathbf{Q}_{\text{AF}}$ ; close triangles: the weight of the AFLRO peak at half filling. The dashed line is the total weight from the exact sum rule, which is rescaled to coincide with the mean-field value at  $\delta = 0$  in order to compare the doping dependence.

where the Bose distribution  $n(\omega) = 1/(e^{\beta\omega} - 1)$ . It means that the total weight of the spin susceptibility is related to an averaged spin number per site. At half filling, it is obviously that  $\langle (S_i^z)^2 \rangle$  is exactly  $1/4$ . At finite doping,  $\langle (S_i^z)^2 \rangle$  should be reduced  $(1 - \delta)/4$ .

In the bosonic RVB mean field state, the total weight can be calculated by

$$W_{\text{total}} = \frac{1}{4N} \sum_{i\sigma} \langle b_{i\sigma}^\dagger b_{i\sigma} \rangle (1 + \langle b_{i\sigma}^\dagger b_{i\sigma} \rangle). \quad (32)$$

By using  $\langle b_{i\sigma}^\dagger b_{i\sigma} \rangle = (1 - \delta)/2$ , we have  $W_{\text{total}} = \frac{1}{8}(1 - \delta)(3 - \delta)$ . At half-filling, the total weight is  $\frac{3}{8}$  as compared to the exact result  $1/4$ . The discrepancy is due to the relaxation of the no double occupancy to a global level in the Schwinger-boson mean-field theory<sup>20</sup>. In Fig. 9, the doping dependence of  $W_{\text{total}}$  is shown with the exact result (dashed line) rescaled at  $\delta = 0$ .

We also show the integrated weight of the resonancelike peak in Fig. 9 (solid curves with full squares), defined by

$$W_{\text{peak}} \equiv \int_{\text{peak}} d\omega [1 + n(\omega)] \chi_L''(\omega). \quad (33)$$

At  $\delta = 0.125$ , the weight of the peak is about 0.09, while the total weight is about 0.314, *i.e.*, nearly  $1/3$  of the total weight is concentrated on the resonancelike peak. In Fig. 9, one can see that with the increase of doping concentration,  $W_{\text{peak}}$  actually gets slightly increased, whereas  $W_{\text{total}}$  is reduced. Namely, the resonancelike peak in the superconducting phase will become even more prominent approaching the optimal doping from the underdoping. On the other hand, as the doping concentration is reduced to zero,  $W_{\text{peak}}$  does not simply vanish. Instead, it approaches to a finite value which precisely coincides with the weight of the delta function at  $\omega = 0$  and  $\mathbf{Q} = \mathbf{Q}_{\text{AF}}$  in the dynamic spin structure function at half-filling, which represents the AFLRO. Earlier on, we have seen that at  $\delta \rightarrow 0$  both  $E_g$  and the width  $\sigma$  of the peak in momentum space go to zero. So the resonancelike peak continuously crosses over to the AFLRO at half-filling.

### III. SPIN DYNAMICS BEYOND MEAN-FIELD APPROXIMATION

#### A. Fluctuations induced by the hole distribution

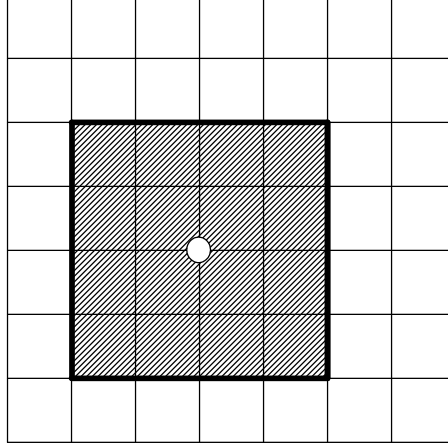


FIG. 10: A way to introduce the gauge-field fluctuations related to the holon density. The open circle denotes a holon. The  $\pi$ -fluxoid bound to the holon is smeared to the shadow area which is smaller than the whole lattice.

In Sec. II C, we have presented a systematic study of the spin dynamics based on the mean-field state of the bosonic RVB description.

The spin dynamics in general is characterized by the effective Hamiltonian (10) which is a gauge model. The mean-field state is obtained by assuming a uniform holon condensation<sup>18</sup> in the superconducting phase such that the topological gauge field  $A_{ij}^h$  may be treated as describing a uniform flux as given in (14). In the previous section, we have found that the spin dynamics is qualitatively modified by such  $A_{ij}^h$  in the superconducting phase, as compared to the AFLRO state at half-filling.

However, an ideal Bose-Einstein condensation is only an approximate description of the holon condensation in the superconducting phase of the bosonic RVB theory. In general, one can expect all kinds of hole density fluctuations. Since the spin degrees of freedom are closely ‘entangled’ with the charge degrees of freedom via  $A_{ij}^h$ , which describes  $\pi$  fluxoids bound to holes according to (11), the spin dynamics will definitely be influenced by such fluctuations. In the following, we examine such an effect.

In the mean-field approximation,  $A_{ij}^h$  characterizes a uniform flux field by smearing out the  $\pi$  fluxoids, bound to holes, over the whole lattice. In this limit, the positions of individual holes are irrelevant. Now we assume a finite size for each smeared  $\pi$  fluxoid, representing some characteristic length scale of coherence for a bosonic holon, which should be still much larger than the average hole-hole distance to reflect the holon condensation (Fig. 10 shows one configuration). Then for a random hole configuration, there is an intrinsic fluctuation in the flux distribution of  $A_{ij}^h$ . With each of such a configuration of non-uniform fluxes, we can follow the steps in last section to get a non-uniform mean-field solution and determine a dynamic spin susceptibility. The dynamic spin susceptibility at  $\mathbf{Q}_{AF}$ , averaged over the random configurations, is presented in Fig. 11, and the local susceptibility  $\chi_L''(\omega)$  is shown in the inset. The result is calculated in a  $16 \times 16$  lattice with each  $\pi$  flux being smeared within a  $14 \times 14$  lattice size, with more than 10,000 configurations being averaged.

For comparison, the mean-field results are plotted as dashed curves in Fig. 11. The main effect of such fluctuations in  $A_{ij}^h$  is to cause the broadening of the resonancelike peak as well as high-energy peaks in energy space, although the peak positions, like  $E_g$ , essentially do not change. Since in the mean-field case, the discrete levels are composed of degenerate Landau levels of  $\xi_m$ , a broadening due to lifting up the degeneracies by the fluctuations in  $A_{ij}^h$  can be easily understood.

In principle, true fluctuations of  $A_{ij}^h$  have to be determined by more closely following the dynamics of holons which in turn is also ‘entangled’ with the spin degrees of freedom. A realistic treatment will thus go far beyond the present scheme. Nonetheless, the above simple-minded approach still provides some valuable insight into the fluctuation issue in the framework of the bosonic RVB theory. In the following, we shall further discuss the momentum profile involved in the low-energy part below  $E_g$ , which will be split from a single sharp peak around  $\mathbf{Q}_{AF}$  after including the fluctuations shown in Fig. 11.

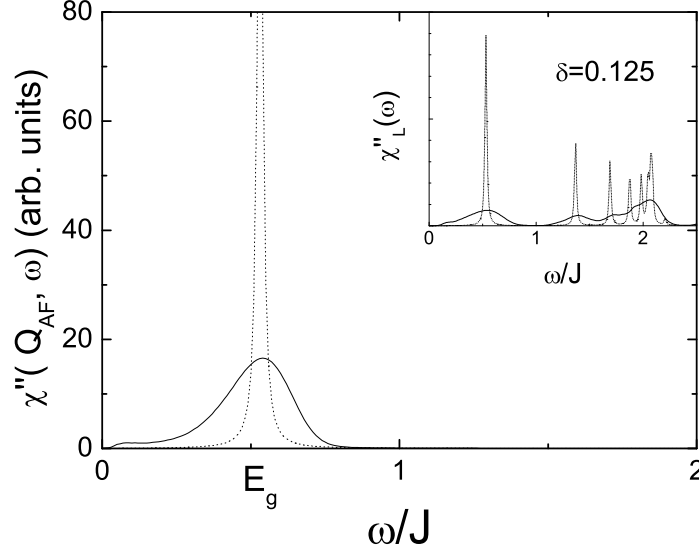


FIG. 11:  $\chi''(\mathbf{Q}_{\text{AF}}, \omega)$  with incorporating the fluctuations induced by the charge degrees of freedom. The doping is at 0.125, and the inset shows the local susceptibility  $\chi''_L(\omega)$  in the same situation.

### B. Incommensurability in momentum space

The bosonic RVB mean-field state is based on the phase string formulation<sup>19</sup> of the  $t - J$  model, in which the short-distance singular part of the phase string effect introduced by the hopping of holes has been ‘gauged away’ such that the Hamiltonian in the new formalism is free of such singularities and thus becomes perturbatively treatable. But when one considers the physical quantities like the dynamic spin susceptibility, such singular effect should be still present in the correlation function and has to be incorporated carefully. It has been shown previously<sup>23</sup> that the leading order contribution of such a singular effect to the dynamic spin susceptibility is simply represented by the incommensurate shifting of the momentum  $\mathbf{Q}$  in  $C_{mm'}(\mathbf{Q})$  defined in (23) by  $\delta Q_x = \pm 2\pi g$  and  $\delta Q_y = \pm 2\pi g$  (taking  $a = 1$ ) with  $g \simeq \delta$ . However, since the momentum width of the resonancelike peak in the mean-field is given by  $\sigma = \sqrt{\pi\delta}$ , the incommensurability does not explicitly show up in the dynamic spin susceptibility<sup>23</sup> and the resonancelike peak still looks like one peak centered at  $\mathbf{Q}_{\text{AF}}$ , as illustrated in the top panel of Fig. 12.

Now, due to the above-discussed fluctuational effect, the resonancelike peak is broadened with some of its weight shifting towards lower energies shown in Fig. 11. The corresponding width for these new low-lying modes in momentum space will be reduced too (*i.e.*, the spin-spin correlation lengths are enhanced at energies lower than  $E_g$ ) such that the incommensurability may become manifested in the dynamic spin susceptibility gradually with the decrease of the energy. Indeed, by using the same simulation used in Fig. 11, the incommensurate peaks do show up in the modified  $\chi''(\mathbf{Q}, \omega)$  with incorporating the incommensurate shifting<sup>23</sup>, as  $\omega$  is lowered below  $E_g$ , which is illustrated in Fig. 12 at  $\delta = 0.125$ .

Therefore, the incommensurability in the dynamic spin susceptibility function is an intrinsic property of the phase string effect<sup>23</sup>. But its visibility crucially depends on spin fluctuations with longer correlation lengths at low energies. Such low-lying spin excitations, induced by the charge density fluctuations discussed above, are usually most prominent in the single-layer case, applicable to the LSCO compound. In contrast, the charge density fluctuations are expected to be weaker in the bilayer systems such as the YBCO compound, where the interlayer coupling will prefer the uniform distribution of the holons as to be discussed in the next section.

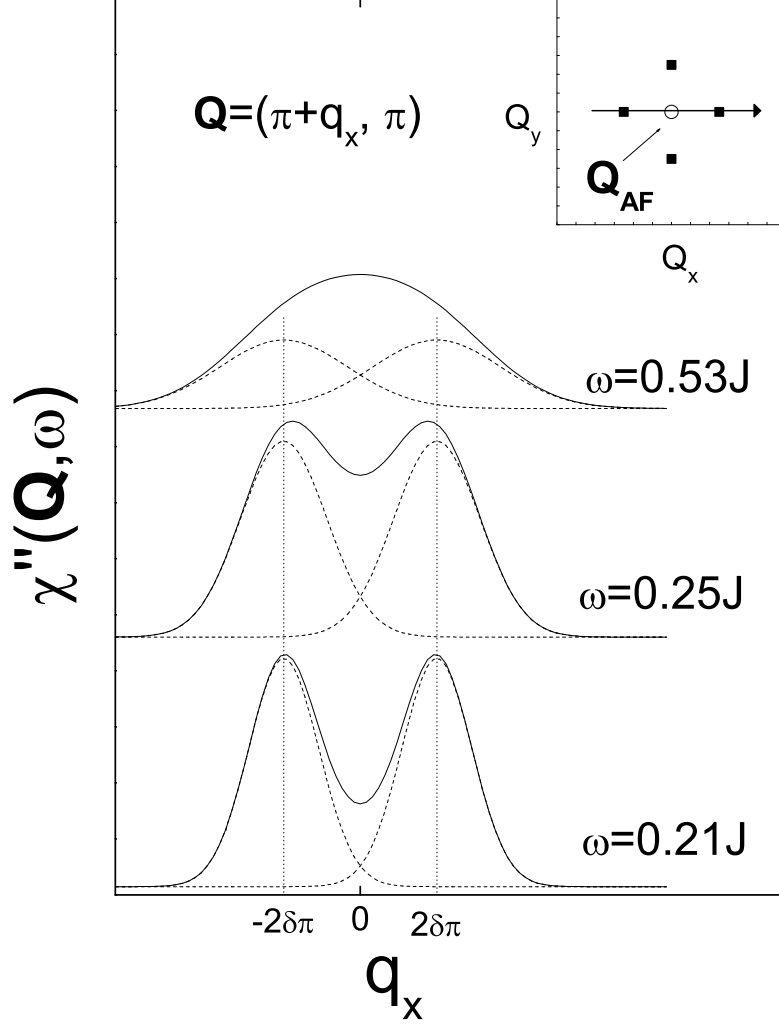


FIG. 12: The incommensurate structure is generally presented in  $\chi''(\mathbf{Q}, \omega)$  due to the phase string effect<sup>23</sup>, but its visibility depends on the energy. The broad commensurate peak at  $\omega = E_g \sim 0.53J$  at  $\delta = 0.125$  is actually composed of four peaks (dashed curves), which becomes visibly ‘split’ in momentum space as  $\omega$  is lowered below  $E_g$ , when the fluctuational effect is included, where the individual peak width is reduced (or spin correlation length is enhanced) .

#### IV. BOSONIC RVB DESCRIPTION WITH INTERLAYER COUPLING

For a bilayer system, the  $t - J$  model can be generalized as

$$\begin{aligned}
 H_{t-J}^{\text{bilayer}} = & -t \sum_{\langle ij \rangle l \sigma} c_{il\sigma}^\dagger c_{jl\sigma} - t_\perp \sum_{i\sigma} c_{i1\sigma}^\dagger c_{i2\sigma} + H.c. \\
 & + J \sum_{\langle ij \rangle l} \mathbf{S}_{il} \cdot \mathbf{S}_{jl} + J_\perp \sum_{i\sigma} \mathbf{S}_{i1} \cdot \mathbf{S}_{i2}
 \end{aligned} \tag{34}$$

in which the additional subscript,  $l = 1, 2$ , is the layer index. By introducing an additional bosonic RVB order parameter

$$\Delta_\perp^s \equiv \sum_\sigma \langle b_{i1\sigma} b_{i2-\sigma} \rangle, \tag{35}$$

and the Bogoliubov transformation

$$b_{i\sigma} = \sum_{mk} \omega_{mk\sigma}(i, l) (u_{mk} \gamma_{mk\sigma} - v_{mk} \gamma_{mk-\sigma}^\dagger) \quad (36)$$

with  $k = \pm$ , the mean-field spinon Hamiltonian can be diagonalized in the holon condensed phase in a procedure similar to Sec. II as given in Appendix A. We find

$$\omega_{mk\sigma}(i, l) = \frac{1}{\sqrt{2}} [\text{sgn}(\xi_m) k]^l \omega_{m\sigma}(i), \quad (37)$$

$$u_{mk} = \sqrt{\frac{1}{2} \left( \frac{\lambda}{E_{mk}} + 1 \right)}, \quad (38)$$

$$v_{mk} = \text{sgn}(\xi_{mk}) \sqrt{\frac{1}{2} \left( \frac{\lambda}{E_{mk}} - 1 \right)}. \quad (39)$$

and the spinon energy spectrum

$$E_{mk} = \sqrt{\lambda^2 - |\xi_{mk}|^2}, \quad (40)$$

in which

$$\xi_{mk} = \text{sgn}(\xi_m) \left( |\xi_m| + \frac{k J_\perp \Delta_\perp^s}{2} \right). \quad (41)$$

In the above,  $\xi_m$  and  $\omega_{m\sigma}(i)$  are the solution of (18), as the counterparts of  $\xi_{mk}$  and  $\omega_{mk\sigma}(i, l)$ , respectively, in the single layer case. Finally, the self-consistent equations of the RVB order parameters and the Lagrangian multiplier  $\lambda$  are given by

$$|\Delta^s|^2 = \frac{1}{4NJ} \sum_{mk} \frac{\xi_m \xi_{mk}}{E_{mk}} \coth \frac{\beta E_{mk}}{2}, \quad (42)$$

$$\Delta_\perp^s = -\frac{1}{2N} \sum_{mk} \frac{\text{sgn}(\xi_m) k \xi_{mk}}{E_{mk}} \coth \frac{\beta E_{mk}}{2}, \quad (43)$$

$$2 - \delta = \frac{1}{2N} \sum_{mk} \frac{\lambda}{E_{mk}} \coth \frac{\beta E_{mk}}{2}. \quad (44)$$

Fig. 13 shows the results obtained by the self-consistent equations as functions of doping concentration (solid lines) at  $J_\perp = 0.1J$ , while the values of  $\Delta^s$  and  $\lambda$  in the single layer case are plotted by the dashed lines for comparison, which only change slightly with the introduction of the interlayer coupling  $J_\perp = 0.1J$ .

In the inset of Fig. 13, the doping dependence of  $\Delta_\perp^s$  is shown at various  $J_\perp$ 's:  $J_\perp = 0.10J, 0.11J$ , and  $0.12J$ . We note that  $\Delta_\perp^s$  is comparable with the interlayer pairing  $\Delta^s$  at half filling, *e.g.*, 0.765 versus 1.157 even though  $J_\perp = 0.1J$  is quite small. This may be attributed to the fact that the in-plane spin-spin correlation length  $\xi$  is very large at half filling, which diverges at zero temperature. As the consequence, spin mismatches between the two layers will involve a large region determined by  $\xi$ , costing a big energy. This effectively enhances the interlayer AF correlations and thus the interlayer RVB pairing  $\Delta_\perp^s$ .

Away from half filling, as shown in Sec. II, the in-plane spin-spin correlation length decreases monotonically with the hole concentration, which results in the reduction of the inflated interlayer AF correlations. Due to the competitive nature between  $\Delta^s$  and  $\Delta_\perp^s$  (one spin cannot be part of two RVB pairs at the same time), with the decrease of  $\xi$ ,  $\Delta_\perp^s$  will diminish much faster than  $\Delta^s$ , as shown in the main panel of Fig. 13 as well as the inset for different  $J_\perp$ 's.

#### A. Spinon spectrum: Bonding and antibonding states

According to (40) and (41), we find that with a finite  $\Delta_\perp^s$ , the original spinon spectrum  $E_m$  in the single-layer case is split into two branches, a bonding state  $E_{m+}$  and an antibonding state  $E_{m-}$ .

The DOS of spinon spectrum at half-filling is shown in the inset of Fig. 14. At  $\delta = 0$ ,  $\xi_m$  reduces to  $\xi_{\mathbf{q}} = -J\Delta^s(\cos q_x a + \cos q_y a)$ . The ground state still has an AFLRO such that  $\lambda = \max(|\xi_{\mathbf{q},k}|) = (2J\Delta^s + \frac{J_\perp \Delta_\perp^s}{2})$ . The



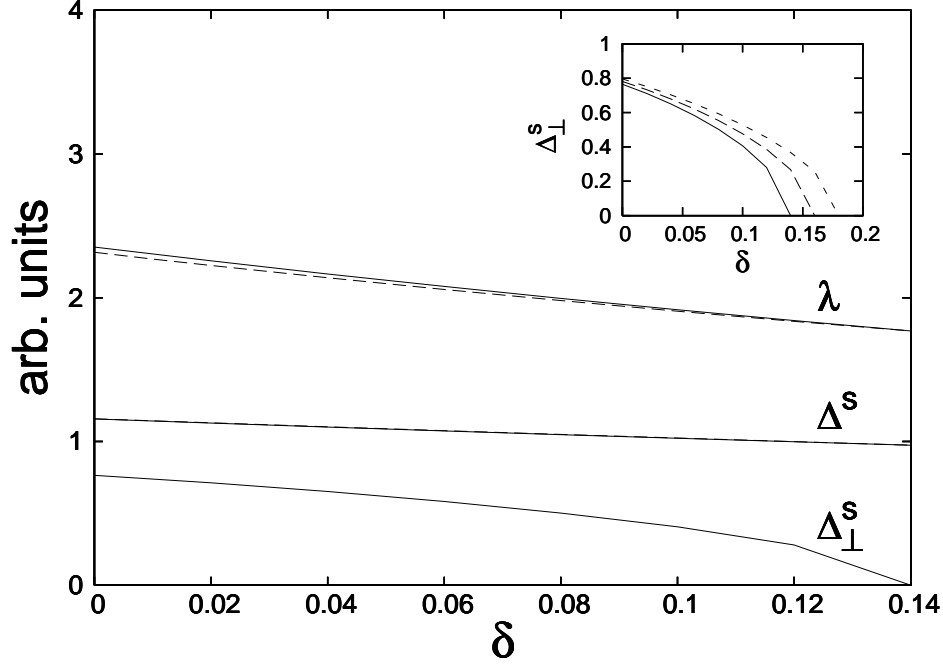


FIG. 13: The doping dependence of  $\Delta_{\perp}^s$ ,  $\Delta^s$ ,  $\lambda$ . The solid line is at  $J_{\perp} = 0.1J$ , the dashed line is the results in the single layer case. The inset is the doping dependence of  $\Delta_{\perp}^s$  at different  $J_{\perp}$ 's: solid line,  $J_{\perp} = 0.10J$ ; dashed line,  $J_{\perp} = 0.11J$ , and dotted line,  $J_{\perp} = 0.12J$

DOS of the bonding states is the same as the single-layer case at  $\omega \rightarrow 0$ , while the antibonding states open a gap  $= \min(E_{m-}) = 2\sqrt{J\Delta^s}\sqrt{J_{\perp}\Delta_{\perp}^s} \sim 0.60J$  at  $J_{\perp} = 0.1J$  as shown by the dashed curve in the inset of Fig. 14. This gap is approximately the same as the gap in the dynamic spin susceptibility in the even channel (see below) as observed by neutron scattering, which is about 70 meV in magnitude<sup>24,25</sup>.

The main panel of Fig. 14 shows the DOS of spinon spectrum at  $\delta = 0.125$  and  $J_{\perp} = 0.1J$  in the superconducting phase. Compared to the spinon spectrum in the single-layer case with the Hofstadterlike structure illustrated by dotted lines in Fig. 14, there are bilayer splittings between the branches of the bonding (solid lines) and antibonding (dashed lines) states, given by  $E_{m-} - E_{m+}$ . Because  $J_{\perp}\Delta_{\perp}^s$  is much smaller than  $\lambda$ , the splitting is most visible at the lowest energy level where  $\xi_m$  is the closest to  $\lambda$ , as shown in the figure. In the following, we study how this bilayer splitting effect is manifested in the dynamic spin susceptibility.

### B. Dynamic spin susceptibility

In the bilayer case, the imaginary part of the spin susceptibility  $\chi''[(\mathbf{Q}, q_{\perp}), \omega]$  depends not only the in-plane wave vector  $\mathbf{Q}$ , but also the c-axis wave vector  $q_{\perp}$ . It can be shown that

$$\chi''[(\mathbf{Q}, q_{\perp}), \omega] = \chi_o''(\mathbf{Q}, \omega) \sin^2(q_{\perp}/2) + \chi_e''(\mathbf{Q}, \omega) \cos^2(q_{\perp}/2), \quad (45)$$

where  $\chi_{o,e}''$  is the imaginary part of the spin susceptibility in the channels with odd and even symmetries, respectively, obtained from the retarded versions of the Matsubara Green's functions defined by

$$\chi_o(i, j; \tau) = -\langle T_{\tau}(S_{i1}^z(\tau) - S_{i2}^z(\tau))(S_{j1}^z(0) - S_{j2}^z(0)) \rangle, \quad (46)$$

$$\chi_e(i, j; \tau) = -\langle T_{\tau}(S_{i1}^z(\tau) + S_{i2}^z(\tau))(S_{j1}^z(0) + S_{j2}^z(0)) \rangle. \quad (47)$$

With the same procedure as in Sec. II C, we can obtain  $\chi_o''$  and  $\chi_e''$  at zero temperature straightforwardly as follows

$$\chi_o''(\mathbf{Q}, \omega) = \frac{\pi}{32} \sum_{mm'kk'} C_{mm'}(\mathbf{Q}) (1 - \text{sgn}(\xi_m \xi_{m'})) kk' \left( \frac{\lambda^2 - \xi_{mk} \xi_{m'k'}}{E_{mk} E_{m'k'}} - 1 \right) \delta(\omega - E_{mk} - E_{m'k'}), \quad (48)$$

$$\chi_e''(\mathbf{Q}, \omega) = \frac{\pi}{32} \sum_{mm'kk'} C_{mm'}(\mathbf{Q}) (1 + \text{sgn}(\xi_m \xi_{m'})) kk' \left( \frac{\lambda^2 - \xi_{mk} \xi_{m'k'}}{E_{mk} E_{m'k'}} - 1 \right) \delta(\omega - E_{mk} - E_{m'k'}). \quad (49)$$

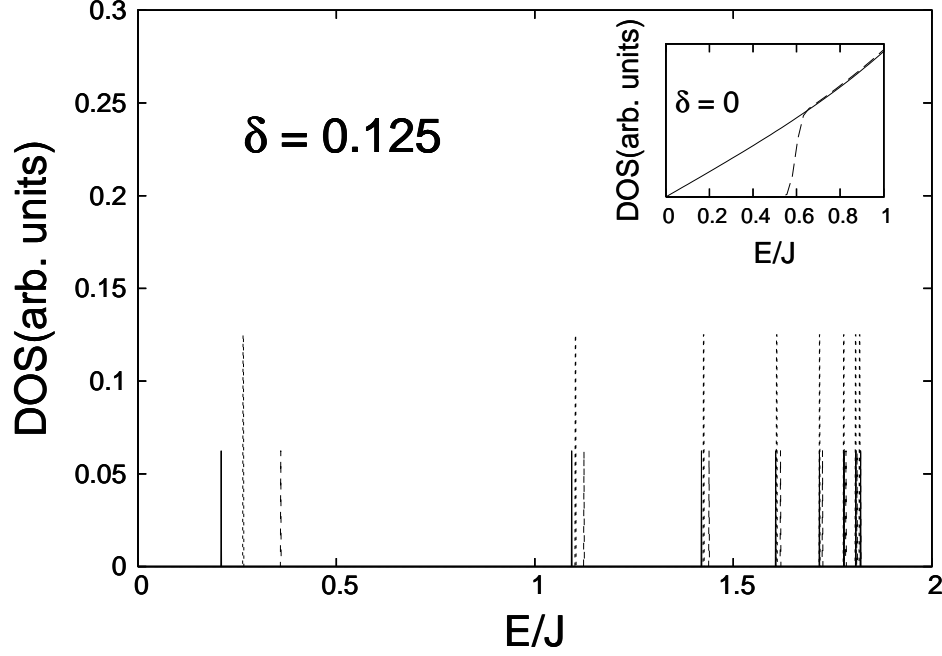


FIG. 14: The DOS of spinons at  $\delta = 0.125$  in the bilayer case. The solid line is for the bonding state, the dashed line for the antibonding state, and the dotted line denotes the single layer case for comparison. The inset shows the bilayer case at half filling: solid curve is for the odd channel and dashed curve is for the even channel.

According to Sec. IIC 3,  $C_{mm'}(\mathbf{Q}_{AF}) = \frac{1}{N}\delta_{m\bar{m}'}$  such that

$$\chi_o''(\mathbf{Q}_{AF}, \omega) = \frac{\pi}{8N} \sum_{mk} \frac{\xi_{mk}^2}{E_{mk}^2} \delta(\omega - 2E_{mk}), \quad (50)$$

$$\chi_e''(\mathbf{Q}_{AF}, \omega) = \frac{\pi}{16N} \sum_{mk} \left( \frac{\lambda^2 + \xi_{mk}\xi_{m-k}}{E_{mk}E_{m-k}} - 1 \right) \delta(\omega - E_{mk} - E_{m-k}). \quad (51)$$

The above expressions clearly show that  $\chi_o''(\mathbf{Q}_{AF}, \omega)$  is solely contributed by a pair of spinon excitations both from the bonding or antibonding states, while  $\chi_e''(\mathbf{Q}_{AF}, \omega)$  is contributed by a pair of spinon excitations, one from the bonding state and the other from the antibonding state. Compared to (25), one can see that  $\chi_o''(\mathbf{Q}_{AF})$  is very similar to  $\chi''(\mathbf{Q}_{AF}, \omega)$  in the single-layer case.

We present the numerical results at  $J_{\perp} = 0.1J$  and  $\delta = 0.125$  in Fig. 15(a) and  $\delta = 0$  in the inset for comparison. The solid curve represents the odd mode while the dashed curve is for the even mode. From the main panel of Fig. 15(a), one sees that the single resonancelike peak in the single-layer case is replaced by a double-peak structure corresponding to the lowest bonding and antibonding states, respectively. In contrast, in the even channel, there is only one peak whose center is just in the middle of the double peaks in the odd channel. We also calculate the local spin susceptibility by integrating over the in-plane wave vector  $\mathbf{Q}$ , which is given in Fig. 15(b). Two figures look quite similar.

The doping dependences of the energies of these peaks are plotted in Fig. 16, where the filled squares mark the double peaks in the odd channel and the open squares describe the peak in the even channel. One finds that the doping dependences for the three peaks are very different. As  $\delta$  tends to zero, the lowest peak in the odd channel behaves like the resonancelike peak and reduces to the gapless spin wave mode at half filling, while the peak at a higher energy in the same channel move to high energy and reaches  $1.190J$  finally.

At last, we consider the effect of the holon fluctuations in the bilayer case by using the same method introduced in Sec. III, and the results are plotted in Fig. 17, in which the solid curve is in the odd channel while the dashed curve is in the even channel. However, we point out that the interlayer coupling should be even more sensitive to the in-plane charge density fluctuations because the nonlocal phase factor involved in  $\Delta_{\perp}^s$  (see Eq.(A7) in Appendix A), which is not considered in Fig. 17. Generally speaking, the in-plane flux fluctuations due to the charge fluctuations will strongly frustrate the interlayer coupling. Thus, in the bilayer system, the former should be suppressed more, as compared to the single-layer case, by the interlayer coupling. More studies along this line will be conducted in future.

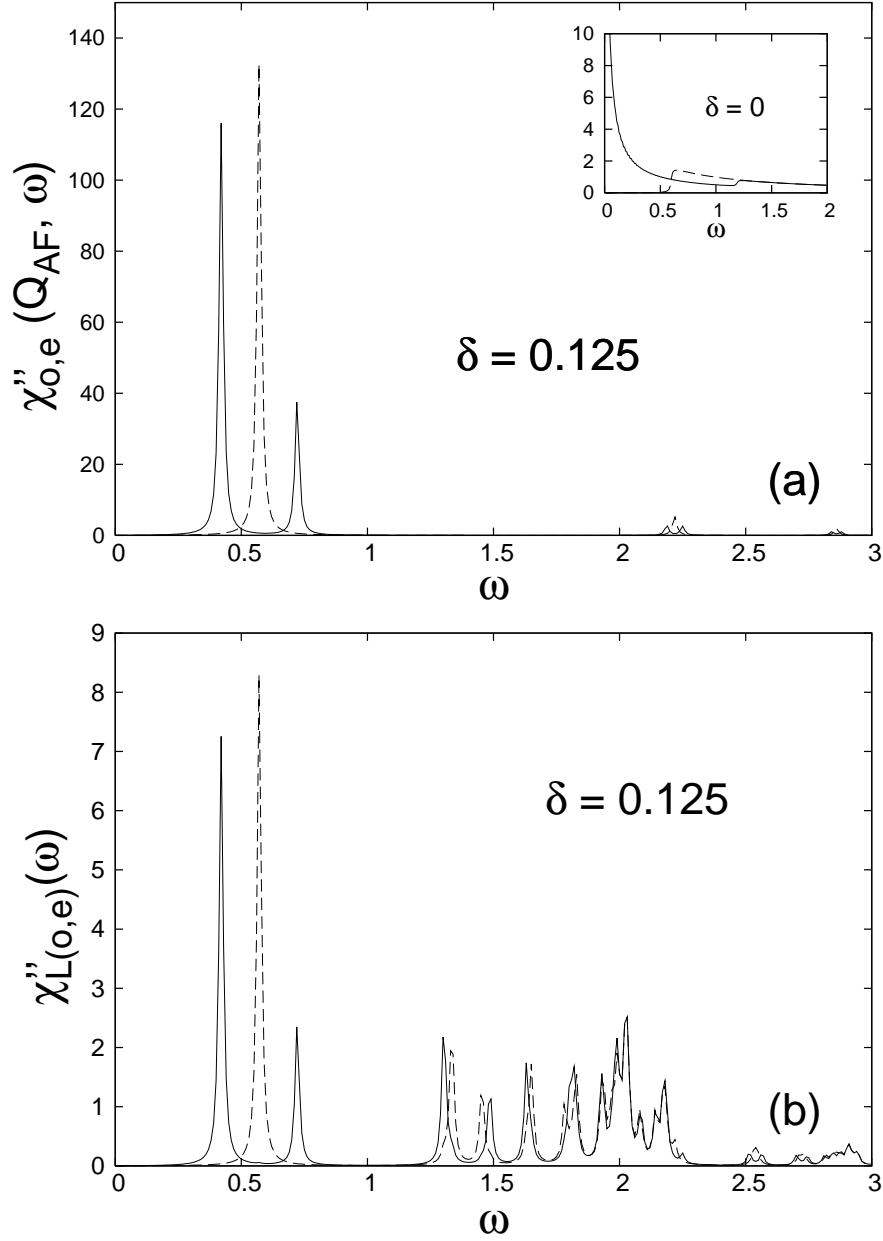


FIG. 15: (a) Dynamic spin susceptibility in the bilayer system at  $\mathbf{Q}_{AF}$  and  $\delta = 0.125$ . The solid line is for the odd channel and the dashed line is for the even channel. The inset is for the half filling case. (b) The local spin susceptibility. The solid curve is for the odd channel, and the dashed curve is for the even channel.

## V. CONCLUSIONS AND DISCUSSIONS

In this paper, we have studied the spin dynamics in the superconducting state of a doped Mott insulator, which is described by the phase string model. In this model, the spin degrees of freedom are characterized by the bosonic RVB mean-field state, which can continuously evolve into the AFLRO state in the zero-doping limit, where the correct spin wave excitations are recovered.

Our study has systematically shown how the low-lying spin wave excitations at half-filling are re-shaped into non-propagating modes in the superconducting phase by the motion of doped holes, via the phase string effect. We have found that the resonancelike peak near the AF wave vectors in the superconducting phase has its dominant spectral weight, at small doping, originated from that of the AFLRO at half-filling. That is, with the opening up a spin gap at finite doping, the low-lying spectral weight, including that of the condensed spinons, is pushed upward to a

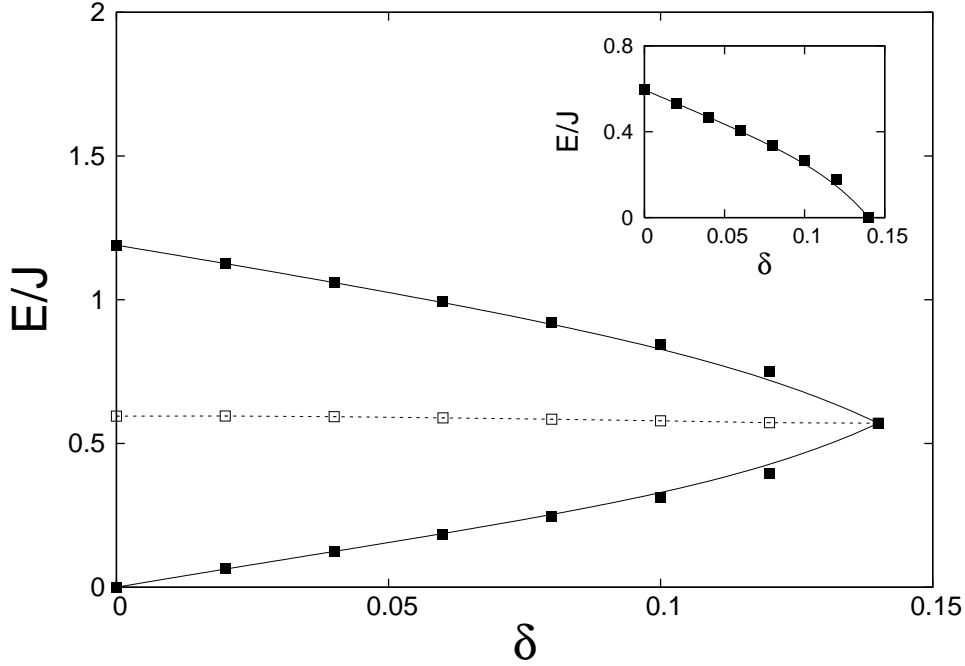


FIG. 16: The energies of the peaks shown in Fig. 15(a) as functions of doping. Close squares: the double peaks in the odd channel; open square: the peak in the even channel. Inset: the difference between the peak in the even channel and the lower energy one in the odd channel.

finite characteristic energy of the resonancelike peak, which is linearly proportional to the doping concentration at small doping. We have analyzed the momentum broadening of the resonancelike peak, which decides a characteristic spin-spin correlation length, inversely proportional to the square root of doping concentration, or the average hole-hole distance.

Our results have also clearly illustrated that the high-energy part of the dynamic spin susceptibility near the Brillouin zone boundary remains essentially the same at half-filling and at small doping, with the high-energy spin-wave signature still present in the superconducting phase. It reflects that fact that the local and high-energy AF correlations, within the length scale of the average hole-hole distance, have not been drastically changed by the motion of the holes. This is in sharp contrast to the prediction based on a Fermi-liquid-like theory, where the Fermi energy will serve as the natural high-energy cutoff in the spin susceptibility function. Our theory suggests that one must combine both the low-lying and high-energy spin excitations in order to correctly understand the nature of the spin dynamics in the high- $T_c$  cuprates.

The fluctuational effects beyond the mean-field theory have also been examined. In the phase string model, the characteristic fluctuations will come from the density fluctuations of holons, which result in the local fluctuations of fluxes attached to holons but seen by spinons. The influence of such fluctuational effect on the spin degrees of freedom has been found to generally cause the broadening of the resonancelike peak in energy space, making the emergence of some low-lying weight below the resonancelike peak. This type of fluctuations is intrinsic and is believed to be important for the single-layer systems like the LSCO compound. In particular, we have found that the spin-spin correlation lengths of these low-lying modes are generally longer than the ‘norm’ one discussed in the mean-field theory. As a consequence, the incommensurability of the spin dynamics at low energies will show up, which is an intrinsic effect of the phase string model but is usually not visible when the width of each peak is too broad in momentum space, as in the ‘norm’ mode at the resonancelike peak.

We have further investigated the interlayer effect on the spin dynamics by considering a bilayer system. At half-filling, the spin excitation spectrum remains the same in the odd channel as the single-layer one at low energy, while a gap is opened up in the even channel, with the magnitude consistent with the experiment. Then we have shown a systematic evolution of the spin excitations, in both odd and even channels, with doping. In the superconducting phase, the effect of the interlayer coupling is most important for the low-lying resonancelike peak near  $\mathbf{Q}_{AF}$ . A prediction for the odd channel is that there will be a second peak with a smaller amplitude emerging at a higher energy, lying between the main resonancelike peak in the odd channel and the peak in the even channel, near  $\mathbf{Q}_{AF}$ . However, both this second peak in the odd channel and the peak in the even channel will be sensitive to the fluctuations *between* the

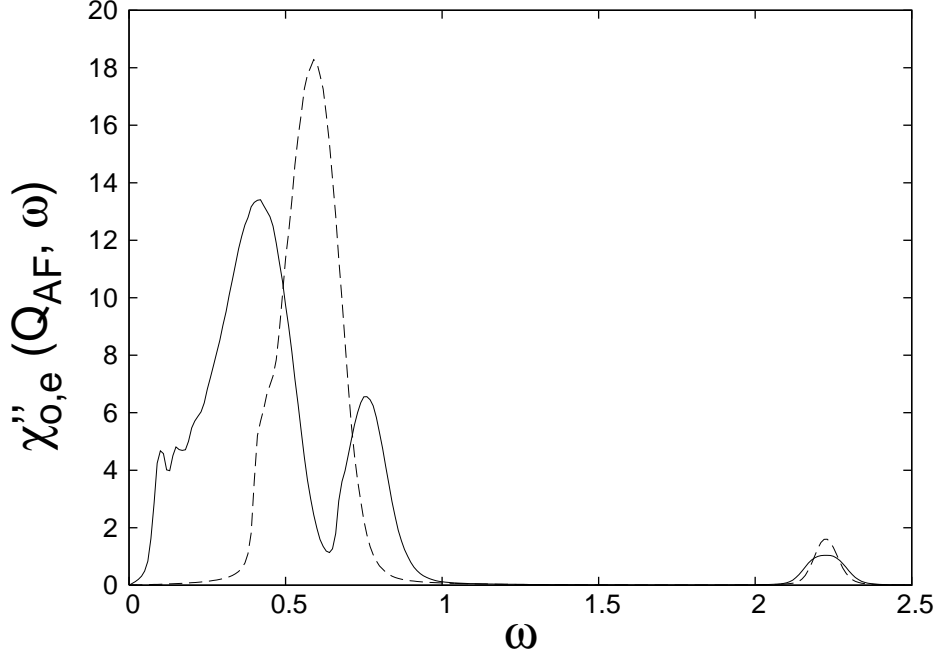


FIG. 17:  $\chi''_{o,e}(\mathbf{Q}_{AF}, \omega)$  with incorporating the in-plane holon fluctuations, simulated in the same way as in Fig.11. The odd mode: solid curve; the even mode: dashed curve.

two layers, which are not included in our mean-field treatment.

Finally, we point out that in the present approach, our main efforts have been focused on the effective Hamiltonian  $H_s$ , which describes the spinon degrees of freedom in the phase string model. The charge degrees of freedom are described by a holon Hamiltonian,  $H_h$ , in the phase string model, which is not considered explicitly as the holons are simply assumed to be Bose condensed in the superconducting phase, and two degrees of freedom are thus decoupled in this sense. But due to the mutual topological gauge fields in the phase string model, the condensed holons can feel an excitation from the spinon degrees of freedom and do response to it, as discussed in Ref.<sup>26</sup>. As a matter of fact, such a response will result in a loose confinement of spinons to allow only the  $S = \text{integer}$  types of spin excitations. We have considered the effect of  $H_h$  within the RPA and ladder-diagram approximations and found that the results presented in this work are not changed essentially, due to the fact that the interactions introduced by  $H_h$  are of logarithmic type and the spinons excitations are localized in space in the superconducting phase. Due to the length of the paper, we shall present these results in a separated paper. Lastly, we remark that the superconducting phase is not stable in the phase string model when the doping concentration is very low ( $< 0.04$ ) where the spin ordered phase will persist, with the doped holes being localized, which have been discussed in Ref.<sup>27</sup> recently.

### Acknowledgments

We acknowledge helpful discussions with Z.C. Gu, T. Li, X. L. Qi, and Y. Zhou. This work is partially supported by the grants of NSFC, the grant no. 104008 and SRFDP from MOE of China.

### APPENDIX A: BOSONIC RVB MEAN-FIELD THEORY FOR THE BILAYER SYSTEM

In the following, we generalize the bosonic RVB mean-field theory for the single-layer case<sup>19</sup> to a bilayer system as described by the generalized  $t - J$  model (34).

We start with the phase string decomposition for the single-layer case<sup>19</sup> with explicitly introducing a layer index  $l$  for each layer ( $l = 1, 2$ ):

$$c_{il\sigma} = h_{il}^\dagger b_{il\sigma} e^{i\Theta_{il\sigma}^{\text{string}}}, \quad (\text{A1})$$

where  $e^{i\Theta_{il\sigma}^{\text{string}}}$  tracks the in-plane phase string effect, defined by

$$\Theta_{il\sigma}^{\text{string}} = \frac{1}{2}(\Phi_{il}^b - \sigma\Phi_{il}^h), \quad (\text{A2})$$

with

$$\Phi_{il}^b \equiv \sum_{j \neq i} \theta_i(j) \left( \sum_{\alpha} \alpha n_{jl\alpha}^b - 1 \right), \quad (\text{A3})$$

and

$$\Phi_{il}^h \equiv \sum_{j \neq i} \theta_i(j) n_{jl}^h. \quad (\text{A4})$$

The exchange term in the phase string formulation reads

$$H_J^{\text{bilayer}} = -\frac{J}{2} \sum_{\langle ij \rangle, l} \left( \hat{\Delta}_{ij,l}^s \right)^\dagger \hat{\Delta}_{ij,l}^s - \frac{J_\perp}{2} \sum_i \left( \hat{\Delta}_{ii,\perp}^s \right)^\dagger \hat{\Delta}_{ii,\perp}^s. \quad (\text{A5})$$

where the in-plane RVB pair order parameter

$$\hat{\Delta}_{ij,l}^s = \sum_{\sigma} e^{-i\sigma A_{ij,l}^h} b_{il\sigma} b_{jl-\sigma}, \quad (\text{A6})$$

and the interlayer RVB pair order parameter

$$\hat{\Delta}_{ii,\perp}^s = \sum_{\sigma} e^{-i\frac{\sigma}{2}(\Phi_{i1}^h - \Phi_{i2}^h)} b_{i1\sigma} b_{i2-\sigma}. \quad (\text{A7})$$

In the single-layer case, the hopping term contributes to an additional feedback effect<sup>18</sup> on the spin degrees of freedom, besides the phase string effect. But it does not qualitatively and quantitatively change the main results of the spin dynamics. Similarly, the interlayer hopping term is not considered here due to the same reason.

In the superconducting state, due to the holon condensation<sup>18</sup>, the in-plane gauge field  $A_{ij,l}^h$  can be treated as describing a uniform flux [*cf.* (14)]. On the other hand, the phase difference between  $\Phi_{i1}^h$  and  $\Phi_{i2}^h$  for two layers may be considered as a constant in the holon condensation case, i.e.  $\Phi_{i1} - \Phi_{i2} = \phi$ , so that it can be gauged away. Then it is natural to introduce the following RVB order parameters

$$\Delta^s \equiv \left\langle \sum_{\sigma} e^{-i\sigma A_{ij,l}^h} b_{il\sigma} b_{il-\sigma} \right\rangle, \quad (\text{A8})$$

$$\Delta_{\perp}^s \equiv \left\langle \sum_{\sigma} b_{i1\sigma} b_{i2-\sigma} \right\rangle. \quad (\text{A9})$$

The superexchange term including the interlayer coupling is thus reduced to

$$\begin{aligned} H_s = & -\frac{J\Delta^s}{2} \sum_{\langle ij \rangle \sigma l} b_{il\sigma}^\dagger b_{jl-\sigma}^\dagger e^{i\sigma A_{ij,l}^h} - \frac{J_\perp \Delta_{\perp}^s}{2} \sum_{i\sigma} b_{i1\sigma}^\dagger b_{i2\sigma}^\dagger + H.c. + \text{const.} \\ & + \lambda \left( \sum_{il\sigma} b_{il\sigma}^\dagger b_{il\sigma} - 2(1-\delta)N \right). \end{aligned} \quad (\text{A10})$$

To diagonalize this Hamiltonian, we introduce the generalized Bogoliubov transformation

$$b_{il\sigma} = \sum_{mk} \omega_{mk\sigma}(i, l) (u_{mk} \gamma_{mk\sigma} - v_{mk} \gamma_{mk-\sigma}^\dagger), \quad (\text{A11})$$

where  $k = \pm$ . By requiring

$$[H_s, \gamma_{mk\sigma}] = E_{mk} \gamma_{mk\sigma}, \text{ and } [H_s, \gamma_{mk\sigma}^\dagger] = -E_{mk} \gamma_{mk\sigma}^\dagger, \quad (\text{A12})$$

we find

$$(\lambda - E_{mk})u_{mk\sigma}(i, l) = -\frac{J\Delta_s}{2} \sum_{j=NN(i)} v_{mk-\sigma}^*(j, l) e^{i\sigma A_{ij}^h} - \frac{J_\perp \Delta_\perp^s}{2} v_{mk-\sigma}^*(i, l') \quad (\text{A13})$$

$$(\lambda + E_{mk})v_{mk\sigma}(i, l) = -\frac{J\Delta_s}{2} \sum_{j=NN(i)} u_{mk-\sigma}^*(j, l) e^{i\sigma A_{ij}^h} - \frac{J_\perp \Delta_\perp^s}{2} u_{mk-\sigma}^*(i, l'), \quad (\text{A14})$$

where  $l'$  denotes the layer different from  $l$ . We obtain the solution

$$u_{mk\sigma}(i, l) = u_{mk}\omega_{mk\sigma}(i, l), \quad v_{mk\sigma}(i, l) = v_{mk}\omega_{mk\sigma}(i, l), \quad (\text{A15})$$

with

$$u_{mk}^2 - v_{mk}^2 = 1, \quad (\text{A16})$$

and  $\omega_{mk\sigma}(i, l)$  satisfies

$$\xi_{mk}\omega_{mk\sigma}(i, l) = -\frac{J\Delta_s}{2} \sum_{j=NN(i)} \omega_{mk-\sigma}^*(j, l) e^{i\sigma A_{ij}^h} - \frac{J_\perp \Delta_\perp^s}{2} \omega_{mk-\sigma}^*(i, l'). \quad (\text{A17})$$

The spinon spectrum is given by

$$E_{mk} = \sqrt{\lambda^2 - \xi_{mk}^2}. \quad (\text{A18})$$

and

$$u_{mk} = \sqrt{\frac{1}{2} \left( \frac{\lambda}{E_{mk}} + 1 \right)}, \quad (\text{A19})$$

$$v_{mk} = \text{sgn}(\xi_{mk}) \sqrt{\frac{1}{2} \left( \frac{\lambda}{E_{mk}} - 1 \right)}. \quad (\text{A20})$$

According to (18), one has

$$\omega_{mk\sigma}(i, l) = \frac{1}{\sqrt{2}} (\text{sgn}(\xi_m)k)^l \omega_{m\sigma}(i), \quad (\text{A21})$$

$$\xi_{mk} = \text{sgn}(\xi_m) \left( |\xi_m| + \frac{kJ_\perp \Delta_\perp^s}{2} \right), \quad (\text{A22})$$

where  $\xi_m$  and  $\omega_{m\sigma}(i)$  are the solutions of (18).

Finally, the self-consistent equations of the RVB order parameters and the Lagrangian multiplier  $\lambda$  can be obtained as follows

$$|\Delta^s|^2 = \frac{1}{4NJ} \sum_{mk} \frac{\xi_m \xi_{mk}}{E_{mk}} \coth \frac{\beta E_{mk}}{2}, \quad (\text{A23})$$

$$\Delta_\perp^s = -\frac{1}{2N} \sum_{mk} \frac{\text{sgn}(\xi_m)k\xi_{mk}}{E_{mk}} \coth \frac{\beta E_{mk}}{2}, \quad (\text{A24})$$

$$2 - \delta = \frac{1}{2N} \sum_{mk} \frac{\lambda}{E_{mk}} \coth \frac{\beta E_{mk}}{2}. \quad (\text{A25})$$

<sup>1</sup> P. W. Anderson, Science **235**, 1196 (1987).

<sup>2</sup> S. Chakravarty, B.I. Halperin, and D.R. Nelson, Phys. Rev. Lett. **60**, 1057 (1988).

<sup>3</sup> J. Rossat-Mignod, L. P. Regnault, C. Vettier, P. Bourges, P. Burlet, J. Bossy, J. Y. Henry, G. Lapertot, Physica C **185-189**, 86 (1991).

- <sup>4</sup> H. F. Fong, B. Keimer, P. W. Anderson, D. Reznik, F. Doğan, I. A. Aksay, Phys. Rev. Lett. **75**, 316 (1995).
- <sup>5</sup> Pengcheng Dai, H. A. Mook, S. M. Hayden, G. Aeppli, T. G. Perring, R. D. Hunt, F. Doğan Science **284**, 1344 (1999).
- <sup>6</sup> H. He, P. Bourges, Y. Sidis, C. Ulrich and L.P. Regnault, S. Pailhès, N.S. Berzigiarova, N.N. Kolesnikov, B. Keimer, Science **295**, 1045 (2002).
- <sup>7</sup> H. F. Fong, P. Bourges, Y. Sidis, L. P. Regnault, A. Ivanov, G. D. Gu, N. Koshizuka, B. Keimer, Nature **398**, 588 (1999).
- <sup>8</sup> S.M. Hayden, G. Aeppli, H.A. Mook, T.G. Perrg, T.E. Mason, S.-W. Cheong, and Z. Fisk, Phys. Rev. Lett. **76**, 1344 (1996).
- <sup>9</sup> M. A. Kastner, R. J. Birgeneau, G. Shirane, Y. Endoh, Rev. Mod. Phys. **70**, 897 (1998).
- <sup>10</sup> K. Yamada, C.H. Lee, K. Kurahashi, J. Wada, S. Wakimoto, S. Ueki, H. Kimura, and Y. Endoh, Phys. Rev. B **57**, 6165 (1998).
- <sup>11</sup> P. Bourges, Y. Sidis, H. F. Fong, L. P. Regnault, J. Bossy, A. Ivanov, B. Keimer, Science **288**, 1234 (2000).
- <sup>12</sup> H. A. Mook, Pengcheng Dai, S. M. Hayden, G. Aeppli, T. G. Perring, F. Doğan, Nature **395**, 580 (1998).
- <sup>13</sup> P. Dai, H. A. Mook, R. D. Hunt, F. Doğan, Phys. Rev. B **63**, 054525 (2001).
- <sup>14</sup> Q. Si, Y. Zha, K. Levin, and J.P. Lu, Phys. Rev. B **47**, 9055 (1993).
- <sup>15</sup> L. Ying, S. Chakavarty, P.W. Anderson, Phys. Rev. Lett. **78**, 3559 (1997).
- <sup>16</sup> J. Brinckmann and P. A. Lee, Phys. Rev. Lett. **82**, 2915 (1999).
- <sup>17</sup> S.C. Zhang, Science **275**, 1089 (1997).
- <sup>18</sup> Z. Y. Weng, D. N. Sheng, C. S. Ting, Phys. Rev. B **59**, 8943 (1999); Phys. Rev. Lett. **80**, 5401 (1998).
- <sup>19</sup> Z. Y. Weng, D. N. Sheng, Y.-C. Chen, C. S. Ting, Phys. Rev. B **55**, 3894 (1997); D. N. Sheng, Y. C. Chen, and Z. Y. Weng, Phys. Rev. Lett. **77**, 5102 (1996).
- <sup>20</sup> D. P. Arovas and A. Auerbach, Phys. Rev. B **38**, 316 (1988); A. Auerbach and D. P. Arovas, Phys. Rev. Lett. **61**, 617 (1988).
- <sup>21</sup> Z.Y. Weng, Y. Zhou, and V.N. Muthukumar, preprint (2004).
- <sup>22</sup> S. Liang, B. Doucot, P. W. Anderson, Phys. Rev. Lett. **61**, 365 (1988).
- <sup>23</sup> Z. Y. Weng, D. N. Sheng, C. S. Ting, Phys. Rev. B **59**, 11367 (1999).
- <sup>24</sup> S. M. Hayden, G. Aeppli, T. G. Perring, H. A. Mook, F. Doğan, Phys. Rev. B **54**, R6905 (1996).
- <sup>25</sup> D. Reznik, P. Bourges, H. F. Fong, L. P. Regnault, J. Bossy, C. Vettier, D. L. Milius, I. A. Aksay, B. Keimer, Phys. Rev. B **53**, R14741 (1996).
- <sup>26</sup> V. N. Muthukumar and Z. Y. Weng, Phys. Rev. B **65**, 174511 (2002).
- <sup>27</sup> S.P. Kou and Z.Y. Weng, Phys. Rev. Lett. **90**, 15700 (2003).